Supplementary Information to *Exceptionally Dense and Resilient Critically Jammed Polydisperse Disk Packings*

Sangwoo Kim and Sascha Hilgenfeldt

Definition of angle order parameter

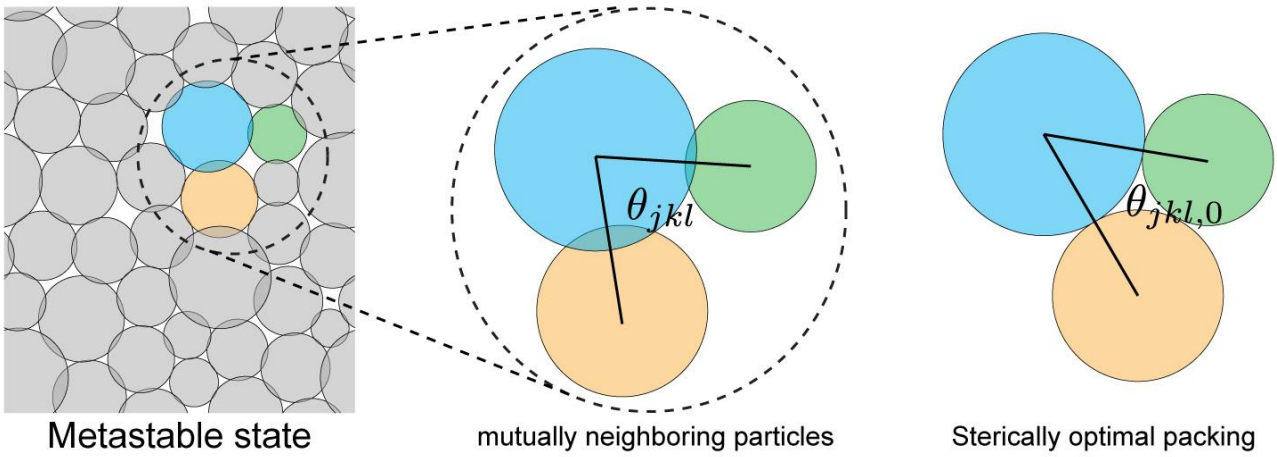

Figure S1: Schematics of a triplet of particles that are mutually neighbors within a metastable state (left and middle), and its corresponding sterically optimal packing. (right)

To quantify structural closeness of particle packings to the reference state of the sterically optimal packing, we employ an angle order parameter. For each particle j with n_j neighbors determined by the radical tessellation, all pairs of neighboring particles, denoted as k and l, are selected, where particles k and l are also neighbors. For every triplet of particles j, k, and l, the angles formed by a line connecting the centers of particles j and k and another line connecting the centers of particles j and l, θ_{jkl}, are measured (Fig. S1). A configuration in which these particles mutually touch each other serves as a reference configuration for the sterically optimal packing. In this optimal packing, the angle between the three particles, $\theta_{jkl,0}$, follows directly from the particle sizes. The angle order parameter for each particle is computed as the average of the absolute difference between θ_{jkl} and $\theta_{jkl,0}$, namely $\Theta_j = \frac{1}{n_j}\sum_{k,l}\left|\theta_{jkl}-\theta_{jkl,0}\right|$. The angle order parameter for the particle packing is defined as the average of the angle order parameters of individual particles.

$$\Theta = \frac{1}{N}\sum_{j=1}^{N}\Theta_j = \frac{1}{N}\sum_{j=1}^{N}\frac{1}{n_j}\sum_{k,l}\left|\theta_{jkl}-\theta_{jkl,0}\right|. \tag{1}$$

Impact of size distribution on the effectiveness of the algorithm

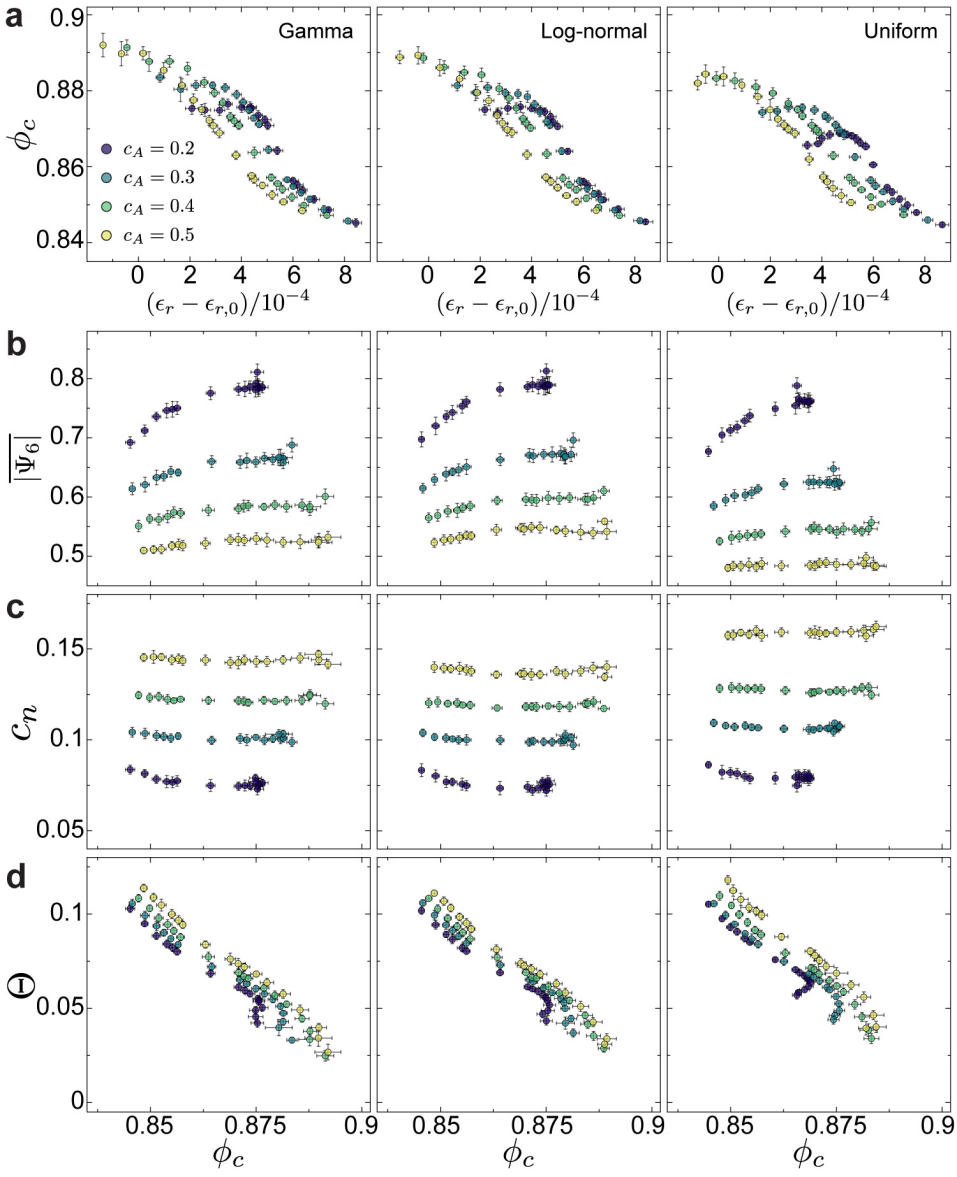

Figure S2: (a) Correlation between energy level of metastable states at $\phi = 1$ and their corresponding critical packing fraction, ϕ_c. Correlations between ϕ_c and structural measures, (b) Hexagonal orientation order parameter $\overline{|\Psi_6|}$, (c) coefficient of variation of radical tessellation topology c_n, and (d) the angle order parameter Θ. In all plots, symbol color distinguishes polydispersity by coefficient of area variation c_A (see (a)). $N = 1024$ for all data.

To assess the impact of size distribution shapes and widths on the algorithm's efficiency, three different distributions - Gamma, Log-normal, and uniform distributions - are tested across a size polydispersity range of $0.2 < c_A < 0.5$. Regardless of the distribution shape and width, the algorithm robustly generates a broad range of critical packing fractions, ϕ_c (Fig. S2a). While conventional structural measures such as $\overline{|\Psi_6|}$ and c_n show weak correlations with ϕ_c (Fig. S2b,c), the angle order parameter Θ is strongly predictive of ϕ_c(Fig. S2d), suggesting that closeness to sterically optimal packing significantly influences the jamming point.

Particle displacement during the annealing process

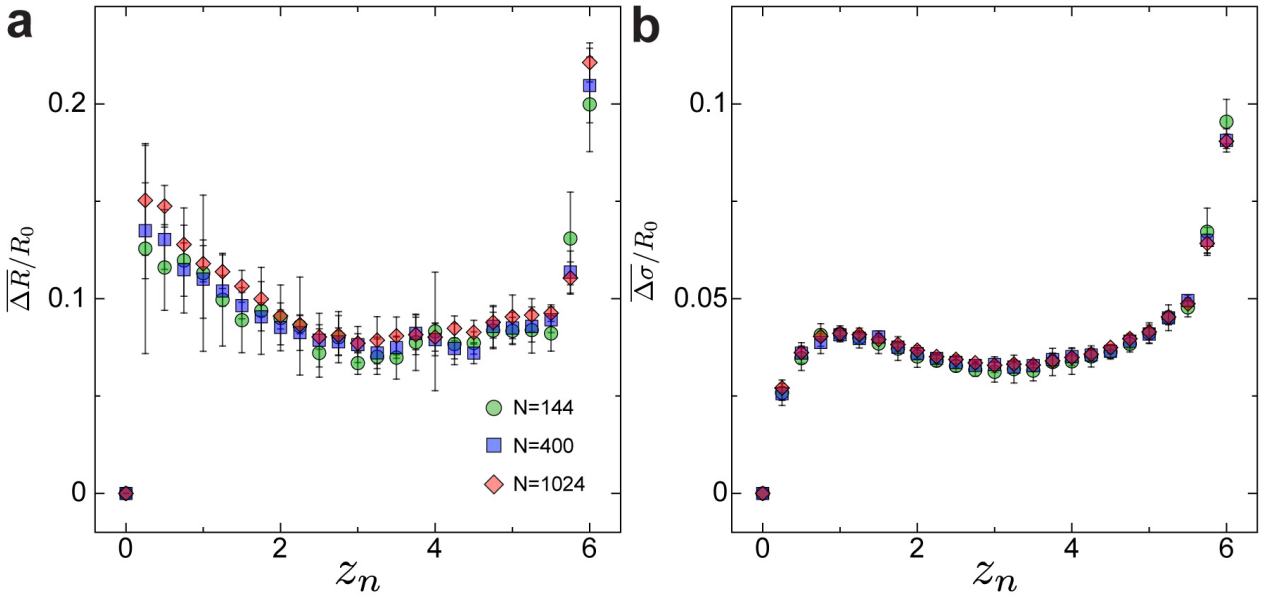

Figure S3: (a) Mean normalized displacement of particles in overjammed packings during the annealing protocol by simultaneous swap. (b) Mean normalized particle size change in overjammed packing during the annealing protocol by simultaneous swap.

The algorithm we propose here performs a single simultaneous size swap, which transitions high energy metastable states to new metastable states of adjustable energy level (the energy of these final metastable states being controlled by z_n). This annealing process involves adjustments of particle positions following the size swap. To quantify the extent of particle motion, we compute the normalized displacement between an initial and a final metastable state following the simultaneous swap and energy minimization (Fig. S3a). Regardless of z_n, the average normalized displacement remains significantly less than 1 (less than a typical particle radius in absolute terms), indicating that local adjustments of particle positions are sufficient to reduce the energy of metastable states from the highest to any arbitrary values, even to the lowest energy level. The magnitude of particle size change during the size swap remains small across the entire range of z_n (Fig. S3b). These slight size changes result in small particle displacements without disrupting the initial topology.

Radial distribution function of critical jamming states of various ϕ_c

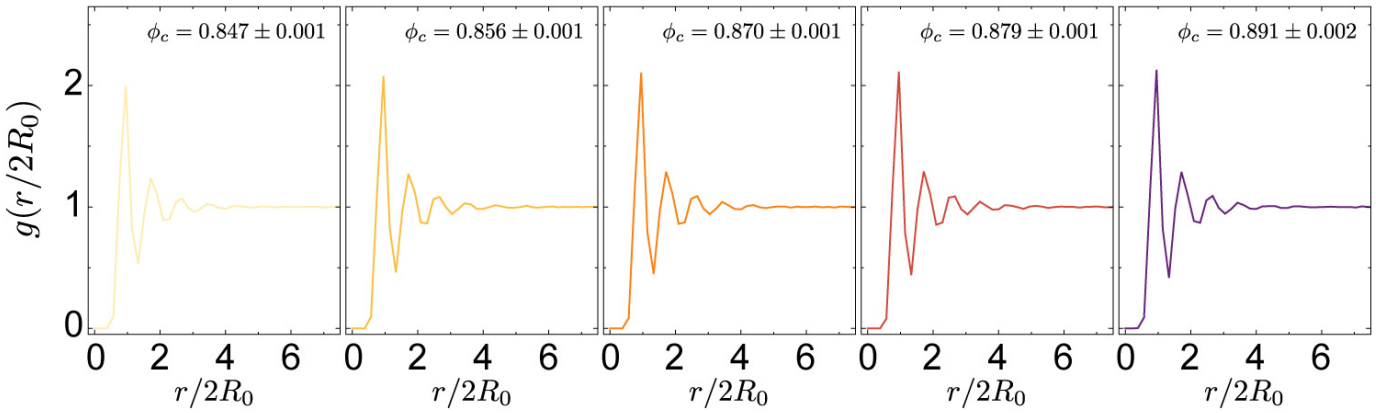

Figure S4: Radial distribution (pair correlation) function of critical jamming states at different ϕ_c, showing no discernible differences. $N = 1024$ for all data.

The radial distribution function, $g(r/2R_0)$ is computed to examine the distinct structural features of critical jamming states across various ϕ_c. While the first peak value of $g(r/2R_0)$ slightly increases with increasing ϕ_c, overall, $g(r/2R_0)$ exhibits minimal variation from the lowest ϕ_c to the highest ϕ_c (Fig. S4). Therefore, we conclude that the radial pair correlation function of particle positions is unsuitable for distinguishing critical jamming states across various ϕ_c.

Efficiency of the annealing algorithm for different ϕ

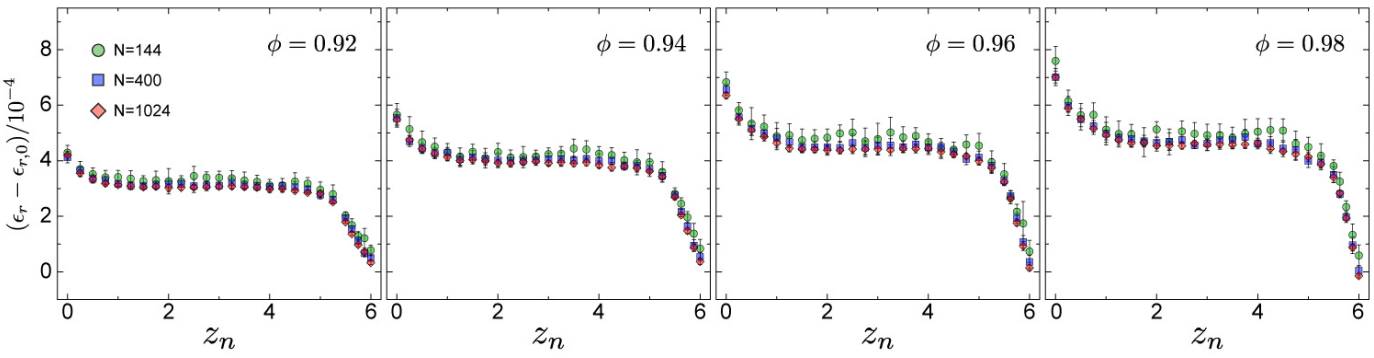

Figure S5: Correlation between average connectivity of network, z_n, and metastable state energy ϵ_r for different volume fraction ϕ.

Although the algorithm is primarily applied to generate metastable states of distinct energy levels at $\phi = 1$ in this work, it can also be utilized to access a broad range of MS energies for arbitrary $\phi > \phi_c$. To evaluate the effectiveness of the algorithm at different ϕ_c, it is tested for four different overjammed packing fractions, $\phi = 0.92, 0.94, 0.96$, and 0.98. For each packing fraction, the algorithm consistently generates metastable states covering the entire range from the highest to the lowest energy level, with the network coordination number z_n remaining a valid control parameter (Fig. S5).

Displacement during the decompression process

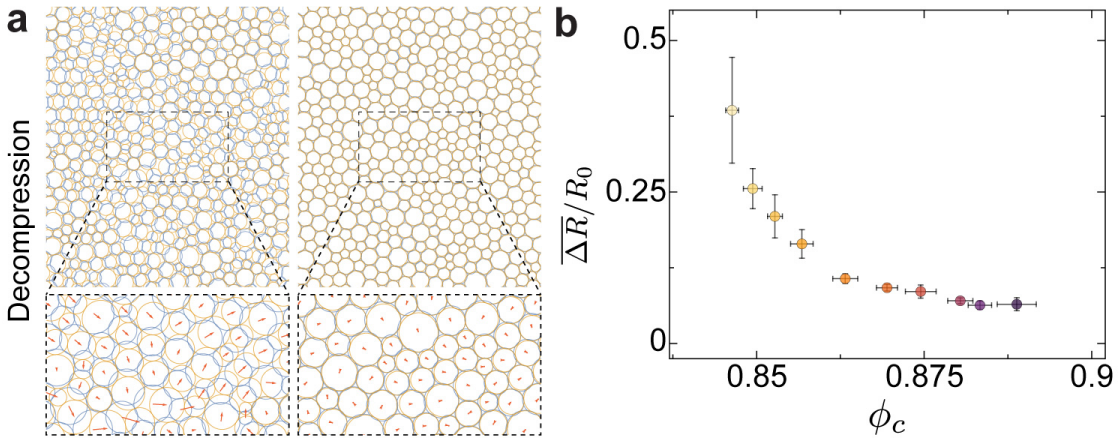

Figure S6: (a) Two examples of the decompression of packings for low (left) and high (right) ϕ_c, with arrows indicating displacements along the decompression. (b) Mean normalized displacement of particles during the decompression process for different initial configurations of final ϕ_n after the decompression. $N = 400$ for all data.

As a supplementary displacement measure for the compression process outlined in the manuscript, we also calculate the normalized displacement during the decompression process from $\phi = 1$ to ϕ_c. Similar to the compression process, high energy metastable states (equivalently low-ϕ_c structures) exhibit high levels of displacement during the decompression process while low energy metastable states (equivalently high-ϕ_c structures) show small displacements, much smaller than a typical particle size. This further supports the conclusion that low-energy MS robustly maintain their structures during mechanical perturbations, whereas high energy MS do not.

Displacement during cyclic pure shear deformation

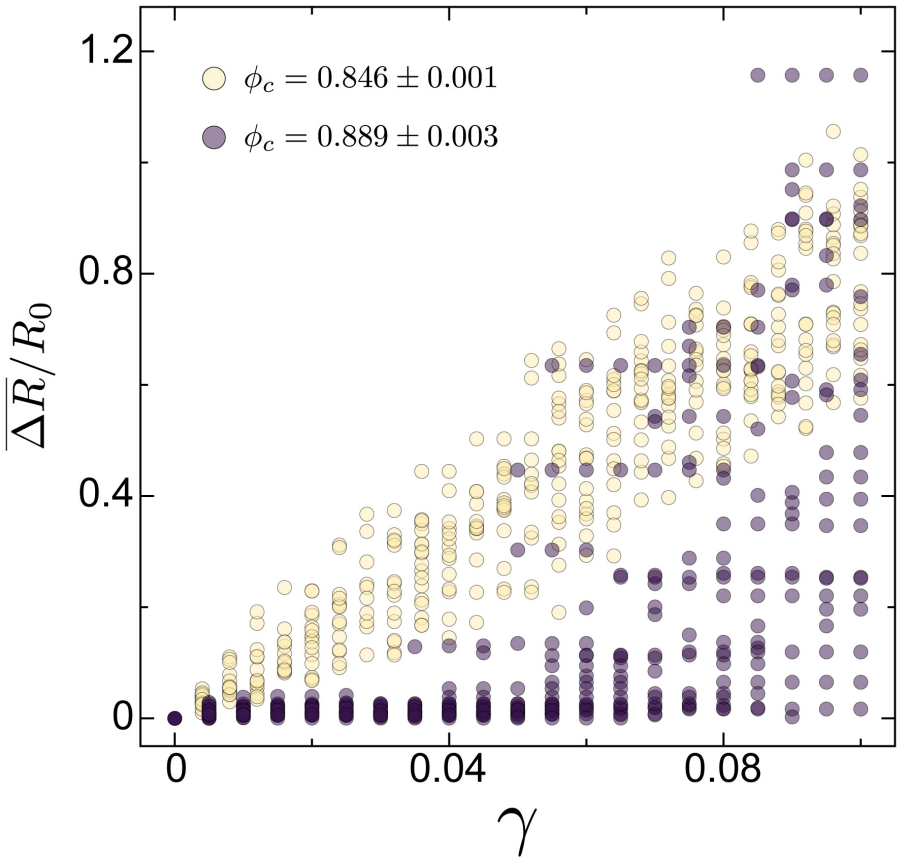

Figure S7: Mean displacement of particles after one cyclic pure shear deformation as a function of strain amplitude γ for low-ϕ_c and high-ϕ_c critically jammed packings. This figure shows results for individual samples rather than the binned averages of Fig. 5f of the main text. $N = 400$ for all data.

Low-ϕ_c critically jammed states exhibit marginal stability under pure shear deformation while high-ϕ_c critically jammed states exhibit prolonged stability up to a finite shear amplitude γ, indicating the resilience feature of dense polydisperse packings. The distinction between low-ϕ_c and high-ϕ_c states persists even for large γ after irreversible rearrangements of particles: many of the individual high-ϕ_c states maintain a new configuration after these rearrangements over a finite range of even higher γ while low-ϕ_c states continuously transition to different states, resulting in a linear increase of mean displacement over the entire range of γ (Fig. S7).

Impact of adjusting the size distribution on critical packing fraction

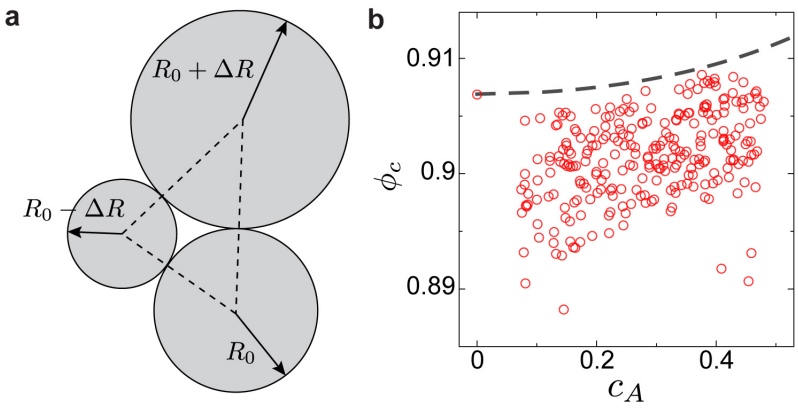

Figure S8: (a) Schematic of a representative locally optimal packing for three particles with a given size variation ΔR. (b) Critical packing fractions, ϕ_c, for structures retaining the modified set of particle sizes after network energy minimization (red circles, system size $N = 400$). Many samples approach and exceed the monodisperse crystalline fraction $\phi_{hex} = 0.9069\ldots$ for significantly large size polydispersity. The gray dashed line indicates the theoretical estimate of the maximum ϕ_c based on the representative configuration shown in (a).

While our primary focus in this work is on the densest packings of a given size distribution (i.e. a fixed set of particle sizes $\{A_i\}$), even higher critical packing fractions ϕ_c of polydisperse disk packings can be achieved if adjustments to the size distribution are permitted. To investigate this, we adapt the original algorithm to retain the adjusted set of sizes after the network energy minimization, $\{A_i'\}$, instead of reassigning the fixed particle sizes $\{A_i\}$, in the order of $\{A_i'\}$. This modification results in a subtly different size distribution from the original one. When applying this algorithm for $z_n = 6$, we observe a significant increase in the accessible range of ϕ_c compared to the original cases (Fig. S8b).

This result is understandable as the adjusted sizes $\{A_i'\}$ specifically optimize local packing (for $z_n = 6$, these are sizes equivalent to those constructed by the Circle Packing algorithm). To estimate a theoretical limit $\phi_{c,max}$ for a given c_A, we consider a sterically optimal triplet packing (Fig. S8a). This packing consists of one particle with an average size R_0, another particle with size $R_- = R_0 - \Delta R = R_0(1 - \Delta r)$, and the other particle with size $R_+ = R_0 + \Delta R = R_0(1 + \Delta r)$. Assuming a Gamma distribution of particle sizes, the normalized deviation Δr can be estimated in terms of the coefficient of variation of particle area, c_A, as follows:

$$\Delta r = \frac{\sqrt{1 - f(c_A)^2}}{f(c_A)}, \tag{2}$$

$$f(c_A) = \frac{c_A \Gamma\left(c_A^{-2} + 1/2\right)}{\Gamma(c_A^{-2})}. \tag{3}$$

The packing fraction of this optimal packing is calculated as the ratio of the sum of disk sectors within the triangle formed by joining the particle centers to the size of the triangle (Fig. S8a). Expanding the angles of

the triangle for small Δr, we can derive an estimate of $\phi_{c,max}$, namely

$$\phi_{c,max}(c_A) = \frac{\pi + \left(\frac{2\pi}{3} - 2\sqrt{3}\right)(\Delta r)^2}{2\sqrt{3(1-(\Delta r)^2)}} \tag{4}$$

This upper-bound estimate is displayed in Fig. S8b and is consistent with the data. We emphasize that such particle-size adjustments are not typically accessible in practical packing problems, where a given set of particles is to be jammed. All results in the main text find rearrangements of such given sets of particle sizes $\{A_i\}$, for various distribution shapes and widths.